CrossMark

Nickel oxide nanocrystals as a lithium-ion battery anode: structure-performance relationship

Abdullah Khalil[1], Boor Singh Lalia[1], and Raed Hashaikeh[1,*]

[1] *Department of Mechanical and Materials Engineering, Institute Center for Water and Environment (iWATER), Masdar Institute of Science and Technology, Abu Dhabi 54224, UAE*

ABSTRACT

Highly crystalline NiO nanocrystals were fabricated via annealing electrospun NiO nanofibers. The fabricated NiO nanocrystals were used as anode material in lithium-ion battery. Electrochemical performance of the NiO nanocrystals was compared with the NiO nanofibers. Differences in the electrochemical performance of NiO nanocrystals and NiO nanofibers were co-related with their morphology, crystallinity, and surface chemistry. NiO nanocrystals-based anodes displayed a specific capacity of about 500 mAh/g under current densities of 100, 200, and 500 mA/g i.e., the specific capacity was found to be independent from current density. In contrast, the specific capacity in the case of nanofibers was found to vary between 500 and 900 mAh/g depending upon the current density. Better consistency was also observed for nanocrystals in terms of long cycle life performance. The improved rate capability and consistency in case of NiO nanocrystals was attributed to the formation of stable nickel phase during the repeated cycling.

Introduction

Since its commercialization by Sony in 1991 [1], lithium-ion battery (LIB) has emerged as the primary source of power for variety of portable electronic devices. The high energy density and minimum self-discharge combined with consistency have made the LIB as the most practical and attractive choice as compared to various other kinds of batteries. Constant and extensive research is being carried out on the design and composition in order to maximize LIB capacity. This involves engineering the anode, cathode, and the electrolyte in between so as to optimize the LIB performance. Among these three constituents of LIB, the anode carries unique significance where the Li ions are stored which travel toward the cathode during the discharge cycle thus causing the flow of current through the external circuit. The anode material should, therefore, possess low reduction potential and high specific capacity. From theoretical perspective, pure Li metal is at the top of the list; however, safety issues and dendrite formation during repeated cycles make the use of pure Li impractical [2]. Thus Li has been employed in various alloyed forms such as Li_3Sb, $Li_{4.4}Si$, and $Li_{4.4}Sn$. The alloying gives better specific capacity; however, their

significant volumetric expansion–contraction during repeated cycling remains an issue [3]. This volumetric instability has been overcome using other inter-metallics such as InSb, Cu_6Sn_5, and Cu_2Sb as anode materials, however at the cost of reduced energy density [4].

Recently, interest has been directed toward conversion reaction where nanostructured metal oxides are incorporated with a carbon-based support matrix and employed as LIB anode. In this case, the following reversible reaction takes place:

$$M_mO_n + 2nLi^+ + 2ne^- <=> nLi_2O$$
$$+ mM \ (M = transition \ metal).$$
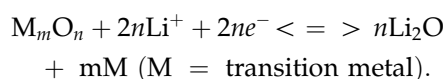
This reaction allows the storage of two or more Li ions per molecule, thus offering high capacity and good cyclability. The use of nano-sized metal oxides in LIB anodes was first demonstrated by Poizot et al., [5] who employed various transition metal oxides such as CoO, NiO, CuO, and FeO and reported capacities up to 700 mAh/g with negligible capacity fading up to 100 cycles. Since then, variety of metal oxides in different nanostructured forms have been employed as LIB anodes and the reported capacity and cyclability has been remarkable [6]. The superior performance of nanostructured metal oxides has been attributed to their large surface area, short diffusion lengths, and an ability to form hierarchical architecture with the support matrix. Despite their excellent performance, the nano-sized transition metal oxides are yet to appear commercially in LIBs due to their high synthesis cost and significant experimental variation as found in the literature.

Various forms of nanostructured metal oxides such as nanoparticles, nanorods, and nanofibers (NFs) have been tested and compared as anode materials for LIBs. For instance, Co_3O_4 NFs with 500 nm diameter grown via template-free method have shown better capacity and cyclability as compared to commercially available Co_3O_4 nanopowder [7]. Similarly, 60–80 nm Fe_2O_3 nanorods synthesized via hydrothermal technique displayed better capacity and cyclability as compared to their micro counterparts [8]. Nanoparticles of different metal oxides such as Fe_2O_3 [9] and ZnO [10] have also shown capacity up to 900 mAh/g with good retention up to 100 cycles. Other specialized morphologies such as hollow nanospheres and nanocubes of Fe_3O_4 [11] and CuO [12], nanosheets of SnO_2 [13] and NiO [14], and hierarchical tubular structures of TiO_2 [15] have also

been investigated as LIB anodes, and their observed superior electrochemical performance has been attributed to their unique architecture and much higher surface area.

Like many other nanostructured metal oxides, nickel oxide (NiO) has gained significant interest as LIB anode material because of its low cost, ease of synthesis, and environment friendly nature. Nanoparticles of NiO have shown reversible capacities in the range of 600–800 mAh/g [16–18]. In case of NiO nanotubes, capacity as low as 200 mAh/g was observed [19]. Other nanostructured forms of NiO such as nanosheets, nanofilms, and nanomembranes have shown much higher capacity in the range of 800–1000 mAh/g with good cyclability [20–22]. Various researchers have also investigated the potential of NiO NFs as LIB anode, and the results have been very encouraging. Su et al. [23] reported the specific capacity as high as 1200 mAh/g even after 100 cycles in case of hydrothermally synthesized NiO NFs. On the other hand, Hyams et al. [24] reported a specific capacity as low as 100 mAh/g for electrochemically grown NiO NFs. However, they also reported that the capacity can be increased to 400 mAh/g, if the NFs are synthesized with lower aspect ratio (i.e., in the form of nanorods).

As far as the metal oxide NF synthesis is concerned, 'electrospinning' has become a popular technique due to its economic and scalable nature [25]. In addition, the process provides excellent control over the morphology (diameter and roughness) of the metal oxide NFs [26, 27]. Thus, NiO NFs have been synthesized via electrospinning and tested as LIB anodes. Aravindan et al. [28] reported the reversible capacity of about 800 mAh/g for electrospun NiO NFs with average diameter of 100 nm. Kundu et al. [29] reported the specific capacity of about 600 mAh/g for electrospun NiO NFs with diameter ranging between 200 and 300 nm. Recently, we observed the specific capacity of about 450 mAh/g with good retention up to 500 cycles for electrospun NiO NFs with average diameter below 50 nm [30].

In the present work, we synthesized the NiO NFs via electrospinning using a solution composed of nickel acetate salt and PVA polymer. These NiO NFs were found to be semi-crystalline and oxygen deficient at the surface. Also, we converted these semi-crystalline NFs into fully crystalline nanocrystals (NCs) via prolonged annealing at high temperature. This annealing also eliminated the oxygen deficiency

leading to nearly stoichiometric surface of the nanocrystals. The performance of these electrospun NiO NFs and NCs was then compared as LIB anodes by combining them separately with flexible and conductive carbon nanostructures (CNS). Understanding the relative behavior of these two nanostructural forms having different morphology, microstructure and composition as LIB anode will pave the way toward optimized performance and hence the commercial usage of nanostructured NiO and other metal oxides in LIBs.

Experimental procedures

Material synthesis

Nickel II acetate (NiAc) and poly(vinyl alcohol) (PVA) (Mw = 61,000) provided by Sigma-Aldrich were used as main chemicals. The solution for electrospinning was prepared by mixing 0.25 g of NiAc in 1 ml of water and 1 ml of acetic acid via magnetic stirring for half an hour. Acetic acid was added to avoid the hydrolysis of PVA. 5 g of 15 wt% aqueous PVA solution was then added, and the solution was left overnight for vigorous magnetic stirring until a viscous and uniform solution was formed. The obtained solution was transferred to a plastic syringe having gage 20 (internal dia = 0.603 mm) stainless steel needle at its end. A Nanon-01A electrospinning setup (MECC, Japan) was used for electrospinning. The nozzle–collector distance, voltage, and solution flow-rate were maintained at 10 cm, 29 kV, and 0.5 ml/h, respectively. The electrospinning was carried out at room temperature ($\sim$25 °C), and the relative humidity of 50–60 % was recorded during the process. The fibers were collected on an aluminum foil and were left over night in a furnace at 80 °C to remove the moisture. The fibers were then calcined in the same furnace at 475 °C for 2 h under ambient conditions to remove the polymeric phase. The heating rate was 5 °C/min and once the calcination cycle was over, the furnace was allowed to attain room temperature before removing the samples. This resulted in the formation of random networks of NiO NFs lying on the aluminum foil. The choice of calcining the nanofibers at 475 °C for completely removing the polymeric phase is based on our previous work where we carried out the TGA analysis of pure PVA and PVA/NiAc as-spun nanofibers [31].

To obtain the NiO NCs, the calcined fibers were annealed at 1000 °C in an alumina crucible for 2 h under ambient conditions. The heating rate was maintained at 5 °C/min and once the annealing cycle was over, the furnace was allowed to reach room temperature before removing the samples. This resulted in the formation of NiO NC clusters which were disintegrated into individual NCs via probe sonication in water for 15 min. The NCs were then separated from water and dried overnight in a furnace at 80 °C to obtain the NiO NCs in the dry powdered form.

Material characterization

The morphology of the NFs and NCs was determined using a high-resolution scanning electron microscope (SEM) (Nova NanoSEM, FEI) operating at 5 kV, whereas their microstructure was examined using high-resolution transmission electron microscope (HRTEM) (Tecnai F20, FEI) operating at 200 kV. The crystallinity and purity was also determined through X-ray diffraction (XRD) (Empyrean, PANalytical) using Cu k-alpha radiation (0.154 nm). The surface chemistry and composition of the material was analyzed using X-ray photoelectron spectroscopy (XPS) (Versaprobe II, Physical Electronics). For XPS, the analysis parameters were as follows: Al k-alpha radiation = 1486 eV, pass energy = 23.5 eV, step size = 0.1 eV, take off angle = 45°, X-ray spot size = 200 microns.

Battery fabrication and testing

Carbon nanostructures (CNS) provided by Applied Nanostructured Solutions (ANS) were used as the support matrix for fabricating the electrodes. The details regarding the CNS synthesis can be found elsewhere [32]. The electrode slurries were prepared by mixing 70 wt% NiO NFs or NCs, 20 wt% CNS, and 10 wt% PVDF in N-methyl-2-pyrrolidone for 24 h via magnetic stirring to obtain a homogeneous suspension. The resulting suspension was then coated on copper foil (acting as a current collector) using a doctor blade and dried in vacuum oven overnight at 80 °C. Specific capacities of the cells were calculated by using weight of the NiO NFs i.e., 70 wt%. The geometric area of the electrode was 2 cm^2 with active material loading of 2–2.5 mg. The dried electrodes were then transferred to argon-filled glove box in

which the moisture and oxygen content was maintained below 0.1 ppm. Coin cell batteries were assembled inside the glove box using NiO NFs or NC-based electrode as an anode and lithium foil as cathode. Glass fiber filter was used as a separator and 1 M(molar) LiTFSI solution in binary mixture of EC:DEC (2:1 v/v) was used as a liquid electrolyte.

Cyclic voltammetry (CV) curves of the half cells were obtained on PGSTAT302 N potentiostat/galvanostat (Metrohm Autolab, Netherlands) in the voltage range of 0.01–3.0 V (vs. Li^+/Li) using a scan voltage of 0.1 mV/s. Impedance spectroscopy curves were also obtained for the batteries from the same instrument in the frequency range of 100 kHz–10 mHz at an AC amplitude of 10 mV. Charge–discharge (C–D) cycling performance of the batteries was determined via BT-2043 battery tester (Arbin Instruments, USA) under different current densities.

Results and discussion

Morphology and microstructure

The morphology of the as-synthesized NiO NFs and NCs as observed from high-resolution SEM is shown in Fig. 1. The NFs possess rough surface with diameter below 50 nm. On the other hand, the NCs possess smooth surface with size ranging from 50 to above 200 nm. Figure 2 shows the HRTEM images along with the corresponding electron diffraction patterns for the single NF and NC under same resolution. It can be seen that the NF is composed of 10–20 nm crystallites held within an amorphous matrix. The fast Fourier transform (FFT) insets also support the presence of both the crystalline and amorphous domains within the NF. The corresponding electron diffraction pattern in the form of concentric rings further confirms the polycrystalline nature of NFs. As far as NCs are concerned, they possess long-range crystallinity as evident from their HRTEM image and the dotted electron diffraction pattern. Figure 3 shows the XRD pattern for the NFs and the NCs where much more intense and sharp peaks for the NCs as compared to NFs confirm the higher and long-range crystallinity in NCs as compared to NFs. Also, a pronounced diffuse hump at low 2-theta in case of NFs clearly reveals the presence of significant amorphous content. Within this hump, two sharp but very low-intensity peaks, at 2-theta = 21.5° and 23.8°, were found to be the representative of (100) and (210) planes, respectively, which is an indication of body-centered cubic (BCC) component. Although NiO is an FCC system, the presence of BCC peaks over an amorphous hump has been reported earlier for NiO nanoparticles due to the size effects [33]. The detailed explanations regarding the possible origin of these peaks can be found in our previous work [31]. Both the NFs and NCs show the maximum counts for (200) plane which is generally the preferred crystalline orientation for NiO crystals [34].

The microstructure of NFs, which is defined by the small crystallites held within an amorphous matrix, can be explained from two perspectives: First, the concentration of NiAc in the solution is quite low i.e., NiAc/PVA ratio of 0.75 wt/wt. When the salt concentration is low, the deficiency of salt molecules will restrict the crystal growth within the NFs and hence smaller crystallites will be formed. Several previous studies have also reported the decreasing crystallite size with decreasing salt concentration [35, 36]. Also,

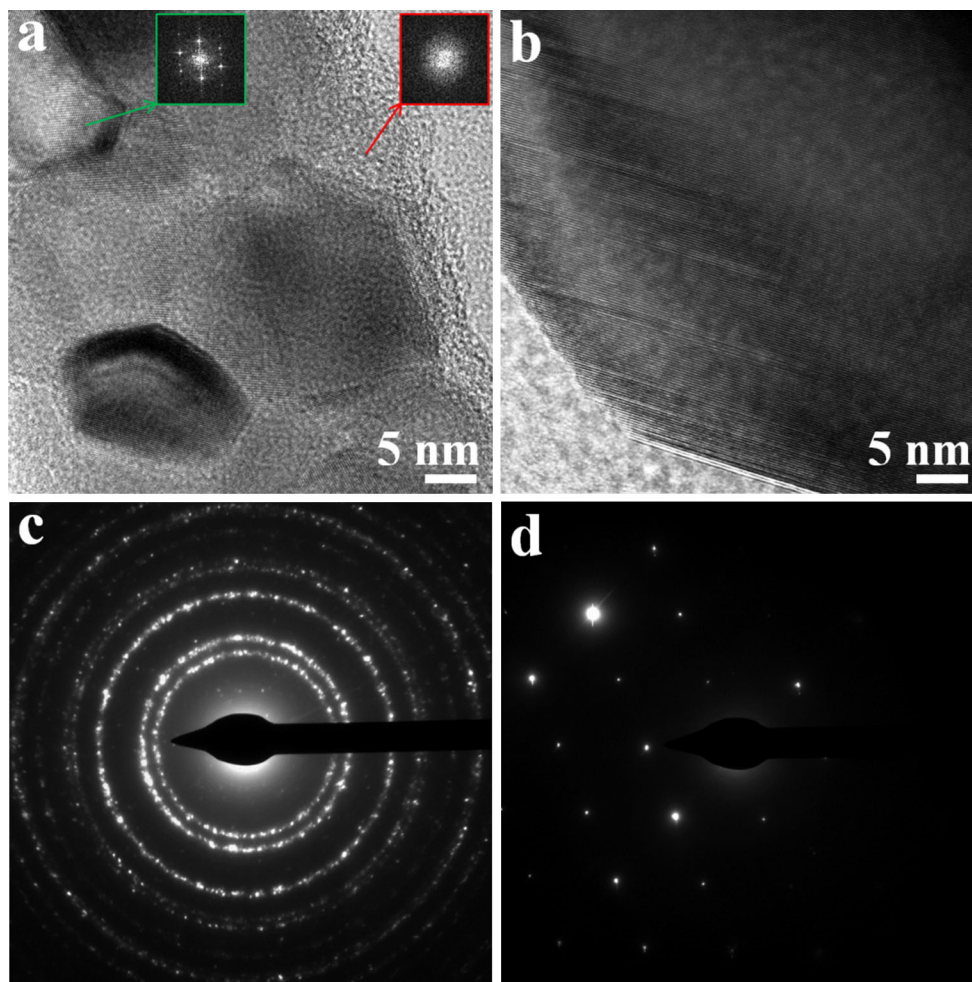**Figure 1** SEM images of electrospun NiO **a** NFs and **b** NCs.
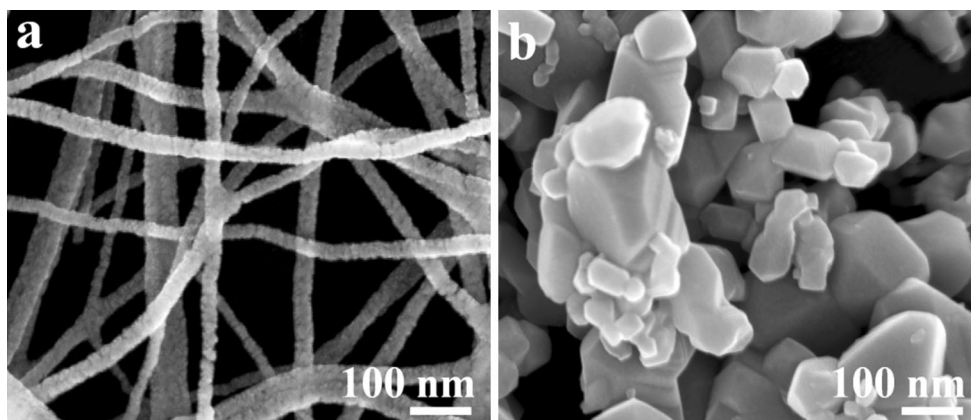
Figure 2 HRTEM images of electrospun NiO **a** NFs (FFT *insets*) and **b** NCs. **c** and **d** Corresponding electron diffraction patterns of **a** and **b**, respectively.
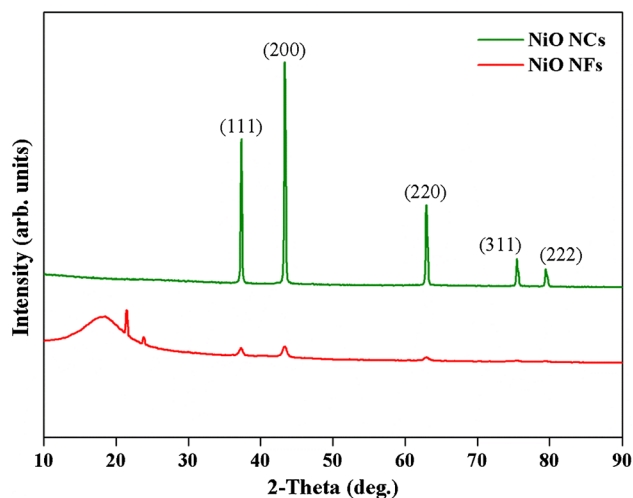

Figure 3 XRD patterns for electrospun NiO NFs and NCs.

the low calcination temperature i.e., 475 °C employed for polymer removal is another likely reason for limited crystal growth. Second, the formation of amorphous NiO can be explained in the context of complex interaction between inorganic and organic phases. It has been suggested that when inorganic phases crystallize within an organic matrix, the crystallization energy dominates over the organic–inorganic interaction energy which does not only stabilize the newly formed small crystal but also the organic–inorganic interface, thus limiting further crystallite growth [37]. When the proportion of organic component is significantly high, such phenomena happening throughout the NFs may cause the formation of tiny crystallites separated by significant volume of amorphous phase (NiO in the

Figure 4 XPS spectra corresponding to **a** O1s and **b** Ni2p$_{3/2}$ transitions for NiO NFs and NCs.
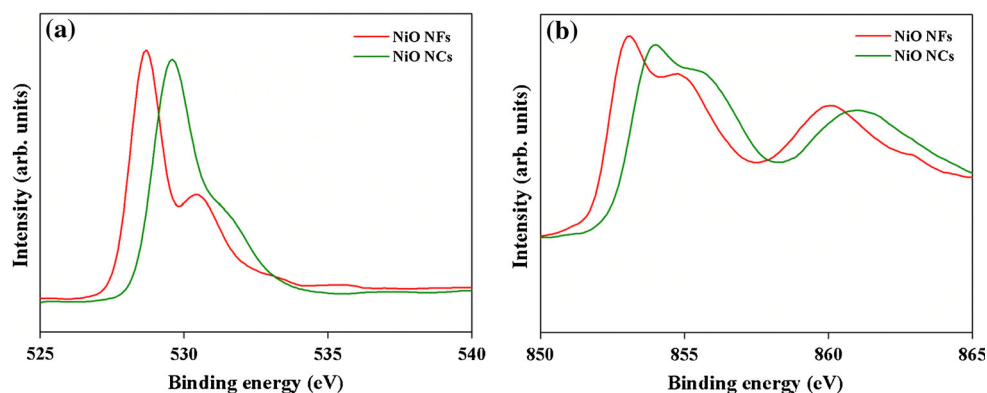
present case). Similar observation has been reported earlier during the synthesis of mesoporous WO_3 using block co-polymer as a structure directing agent where the structure of WO_3 was found to change from large pore-highly amorphous to small pore-highly crystalline with decreasing polymeric content [38].

The transformation of thin and partially crystalline NiO NFs to thick and fully crystalline NiO NCs upon annealing at 1000 °C occurs due to accelerated diffusion leading to merging of several tiny crystallites into one large crystal. Also, the presence of amorphous content between the crystallites will further aid the sintering process as reported elsewhere [39]. The greater size distribution in NCs is due to the random merging of crystallites across the NFs and the subsequent random collapse of the NF structure at various locations. This leads to the formation of NC clusters consisting of randomly sized NCs. Thus, the current observation signifies the fact that the electrospinning technique is not only capable of producing ceramic NFs, but also the ceramic NCs which can be obtained through appropriate heat treatment of electrospun ceramic NFs. The narrow size distribution of NCs, however, remains as a challenge.

Surface analysis

Figure 4 shows the XPS spectra corresponding to O1s and Ni2p$_{3/2}$ electronic transitions for the NiO NFs and NCs. Significant differences can be observed between the NFs and NCs in terms of peak position as well as the peak shape for both the O1s and Ni2p$_{3/2}$ transitions. Table 1 shows the corresponding relative surface composition of Ni and O for the NFs and NCs where it can be seen that the relative percentage

Table 1 Relative surface composition of NiO NFs and NCs as determined via XPS

NiO type	Ni (wt%)	Ideal	O (wt%)	Ideal
NFs	81.95 (±2.31)	78.60	18.05 (±2.31)	21.40
NCs	77.02 (±2.52)		22.98 (±2.52)	

of Ni and O on the surface of the NFs and NCs is noticeably different. In the O1s spectra for NFs, the shift in peak toward lower binding energy (BE) of 528.5 eV followed by a low-intensity peak at 530.5 eV suggests that the charge state of O is closer to that of atomic O [40], and that O exists in multiple oxidation states [41]. In case of NCs, the O1s peak lies at nearly 530 eV which corresponds to fully bonded lattice O with oxidation state of −2. In addition, a diffuse shoulder at around 531.5 eV suggests the presence of chemisorbed O at the surface [42]. As far as the Ni2p$_{3/2}$ spectra are concerned, the NFs again show the slight peak shift toward lower BE of 853 eV, followed by a low-intensity peak at higher BE of about 855 eV. In case of NCs, the high-intensity Ni2p$_{3/2}$ peak lies at nearly 854 eV, with a diffuse shoulder at about 855 eV. These similar observations for Ni2p$_{3/2}$ and O1s spectra for the NFs and NCs suggest incomplete bonding and a more non-stoichiometric surface of the NiO NFs as compared to the NCs.

For various ceramic nanostructures, such as TiO_2 [43] and Fe_2O_3 [44], it has been shown that if the size is quite small, the surface usually contains large number of uncoordinated sites resulting in a surface full of point defects. In general, the surface of ceramic nanostructures is O deficient causing an imbalance in surface stoichiometry, whereas the core remains unchanged with nearly perfect stoichiometry [45].

Such disturbance in surface stoichiometry leads to nearly amorphous surface making the nanomaterials much more active as compared to their bulk counterparts. Our HRTEM observation in Fig. 2a clearly reveals that the NiO NFs are formed through the merging of nanocrystalline domains held together via an amorphous interface. This amorphous part also dominates on the NF surface leading to thermodynamically instable and O-deficient surface. On the other hand, the relative proportion of Ni and O in the NCs in a perfect stoichiometric ratio suggests their thermodynamically stable surface which is same in composition and structure as that of the bulk which is also evident from the HRTEM image in Fig. 2b. Thus the high temperature and prolonged annealing in ambient air does not only transform the semi-crystalline NiO NFs into fully crystalline NCs but also eliminates the O vacancies leading to perfectly stoichiometric NiO NCs.

Cyclic voltammetry

Figure 5 presents the (CV) curves for NiO NFs/CNS and NiO NCs/CNS as LIB anode material. During the first cycle, an intense irreversible peak at 0.25 V for both materials is due to the formation of solid-electrolyte interphase (SEI) layer formation on the electrodes surface which is a common phenomenon in LIBs [46]. This peak, which also represents the anodic current peak (I_{pa}), shifts to 1 and 1.2 V during the next cycles for the anodes based on NiO NFs and NCs, respectively. Also, the value of I_{pa} is much lower and more consistent for NCs as compared to NFs for the 2nd and 3rd cycles. This shows that the reaction between NiO and Li$^+$ ions is less intense but more consistent for NiO NCs as compared to NiO NFs. The redox peak at 2.3 V which also represents

the peak cathodic current (I_{pc}) for both the NFs and NCs correspond to the conversion reaction between NiO and Li [47]. Again, the consistency in case of NCs is evident showing more consistent electrochemical performance of fully crystalline NiO NCs as compared to semi-crystalline NFs.

Charge–discharge performance

Figure 6 presents the charge–discharge (C–D) curves for the NiO NFs/CNS and NiO NCs/CNS as LIB anode material cycled at a current density of 200 mA/g. It can be seen that the maximum specific capacity obtained after 10 cycles for NFs and NCs is about 700 and 500 mAh/g, respectively. The capacity loss from first cycle to tenth cycle is much higher in case of NCs as compared to NFs which shows greater structural changes in NC-based anode during the repeated cycling. The specific capacity for the first 50 cycles at different current densities for the NFs and NC-based anode is presented in Fig. 7. It is evident that the specific capacity, in case of NFs, does not only vary significantly from cycle to cycle but also strongly dependent upon the current density. As can be seen, after 50 cycles, the capacity is only about 400 mAh/g when charged at the current density of 500 mA/g which increases to nearly 900 mAh/g when charged at the lower current density of 100 mA/g. In contrast, the capacity in case of NCs does not only remain similar from cycle to cycle but also interesting to observe is the near independence of capacity from the current density. After 50 cycles, the capacity remains at nearly 400 mAh/g at different current densities.

Figure 8 compares the Coulombic efficiency for the NiO NFs and NC-based anodes under different current densities during the first 10 cycles. The efficiency

Figure 5 CV curves for **a** NiO NFs/CNS and **b** NiO NCs/CNS as anode with Li metal as cathode.
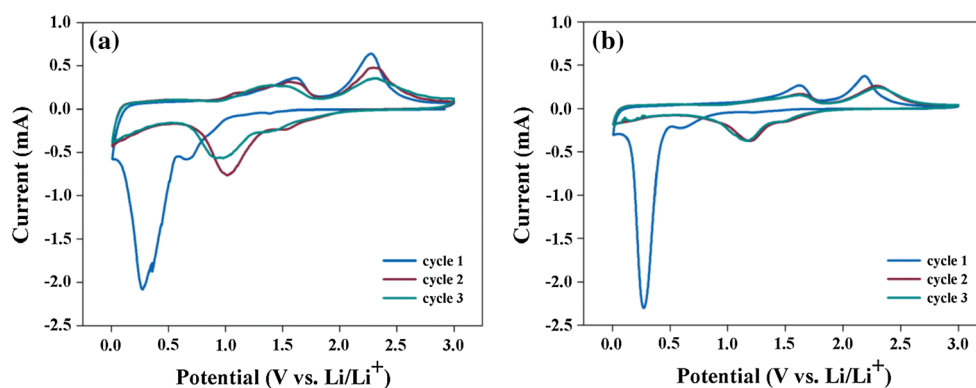
Figure 6 C–D curves for **a** NiO NFs/CNS and **b** NiO NCs/CNS as anode with Li metal as cathode.
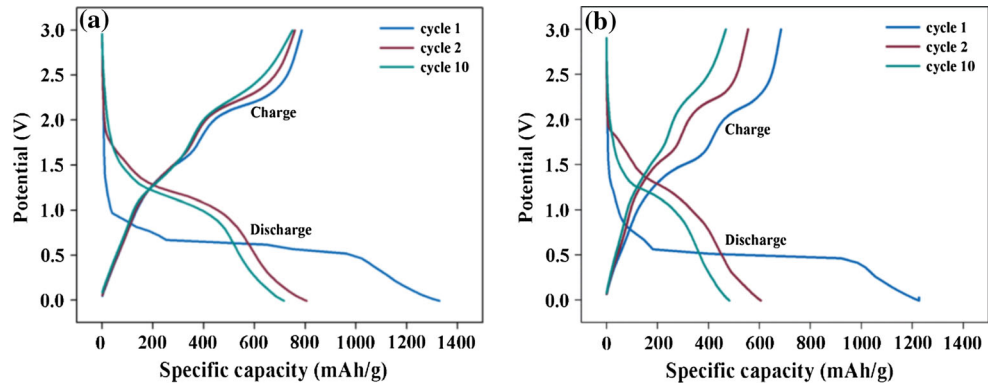

Figure 7 Specific capacity under different current densities for **a** NiO NFs/CNS and **b** NiO NCs/CNS as anode with Li metal as cathode for the first 50 cycles.
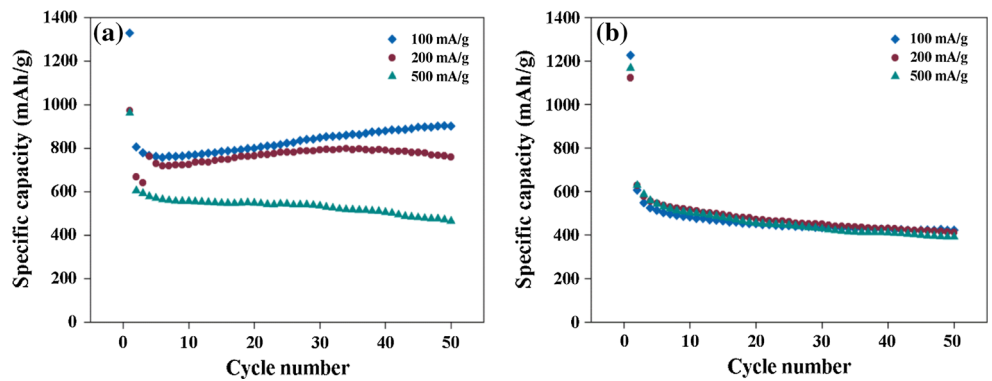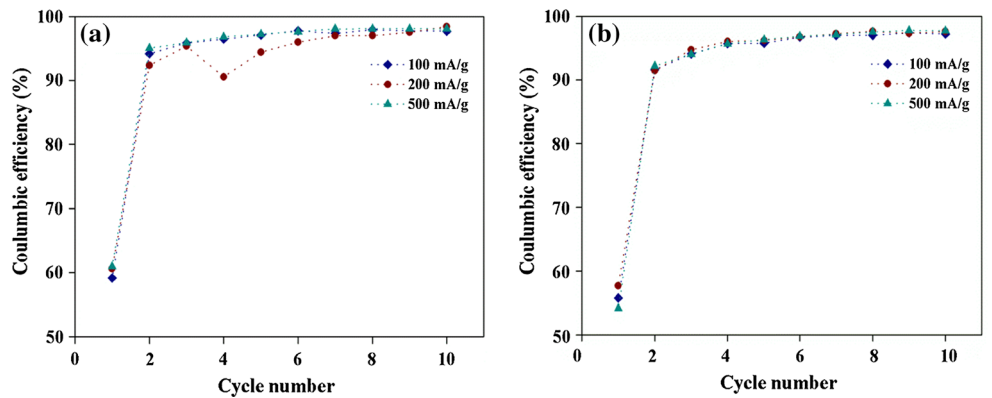

Figure 8 Coulombic efficiency under different current densities for **a** NiO NFs/CNS and **b** NiO NCs/CNS as anode with Li metal as cathode for the first 10 cycles.

is slightly higher for the NFs as compared to the NCs (60 vs. 55 %) during the first cycle which is due to their greater reactivity and better charge transfer capability. This is also supported by a slightly higher specific capacity for the NFs as compared to the NCs during the first discharge (1300 vs. 1200 mAh/g). Greater consistency in efficiency for the subsequent cycles under different current densities in case of NiO NCs can also be observed. Figure 9 compares the rate capability for the two materials where it can be seen

that the capacity in case of NFs drops from about 900 to 500 mAh/g as the C-rate increases from 0.1 to 0.6. In contrast, the capacity remains at about 400 mAh/g irrespective of the C-rate in case of NCs. These observations strongly support the more consistent and repeatable performance of NiO NCs as Li-ion battery anode material.

Figure 10 compares the long cycle life performance for the NFs and NC-based anodes. For NFs, the capacity fades to nearly half during the first 100
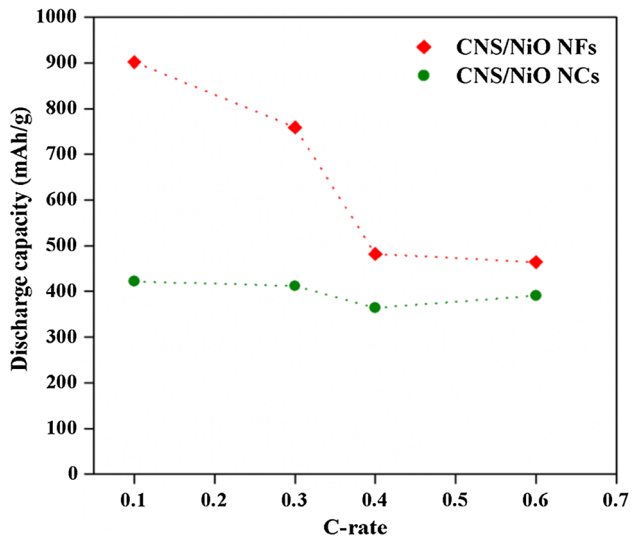
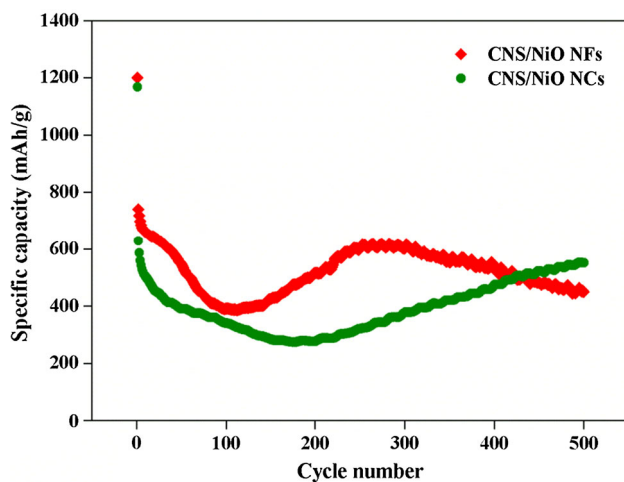**Figure 9** Rate capability for NiO NFs/CNS and NiO NCs/CNS anodes.

Figure 10 Long cycle life performance for NiO NFs/CNS and NiO NCs/CNS anodes.

cycles after which it increases again and reaches a maximum of 600 mAh/g followed by again a decrease to about 450 mAh/g after 500 cycles. In case of NCs, the capacity continues to fade from 600 to about 250 mAh/g during first 200 cycles after which it starts increasing and reaches a maximum value of about 550 mAh/g after 500 cycles. It is interesting to note that the capacity in case of NCs remains lower as compared to NFs till about 420 cycles after which the capacity for NCs exceeds that of NFs. This anomalous behavior of electrodes during cycling is mainly due to the continuous microstructural changes within the

electrodes. During each charge–discharge cycle, the conversion reactions occur, leading to the modification of electrode at the microstructural level. As a result, the electrodes do not exhibit a consistent specific capacity over the large number of cycles as evident from Fig. 8. Similar behavior for NiO-based anodes has been reported in literature even for 50–00 cycles [48–51]. To the best of our knowledge, long cycle life behavior up to 500 cycles or more for NiO has not been studied so far.

Impedance spectroscopy

Figure 11 shows the impedance curves in the high and low-frequency regimes for the batteries which were freshly fabricated from NiO NFs and NC-based anodes. As evident from the intercept of semicircle on the real axis in the low-frequency region, the charge transfer resistance in case of NCs is nearly five times as compared to NFs (250 vs. 50 Ω). This difference clearly shows much higher charge transfer resistance in case of NCs leading to their lower specific capacity. However, slightly higher slope of the line in the low-frequency region for NF-based anode shows its greater ion diffusion resistance (Warburg's resistance) within the electrode. The obtained impedance spectroscopy results are comparable to the results obtained previously by Yuan et al. while studying the electrochromic performance of porous and dense NiO films fabricated via self-assembled monolayer electrodeposition [52]. They found that both the charge transfer and Warburg's resistance are much higher in case of dense NiO films as compared to porous NiO films which signifies the importance of high surface area for improved charge transfer performance. In our case, the average specific surface area of NiO NFs measured via BET was found to be 19.2 m^2/g as compared to only 4.1 m^2/g in case of NCs. Such high surface area of NiO NFs as compared to NCs also explains their lower charge transfer resistance and hence improved capacity as also observed in several studies related to NiO films [53, 54].

Microstructural analysis of anodes

In order to understand the difference between the electrochemical performance of NFs and NCs, SEM and TEM analysis were carried out for the cycled electrodes. Figure 12 shows the SEM images of
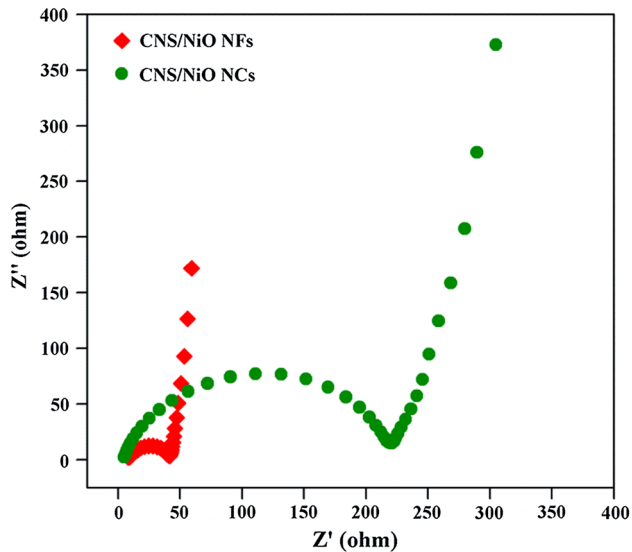
Figure 11 Impedance curves for NiO NFs/CNS and NiO NCs/CNS anodes.

freshly prepared and 50 cycles undergone NiO NFs/CNS and NiO NCs/CNS electrodes. In case of NFs, it can be seen that the NF structure is lost after cycling and the CNS merge with NFs to form an integrated network of NiO and CNS. As far as NiO NCs/CNS electrode is concerned, the NCs also do not exist

anymore and the electrode seems to comprise of CNS uniformly coated with Ni. An important observation, however, in case of NCs is the extensive cracking of electrode causing frequent macroscopic separation across the electrode. This may be attributed volumetric expansion–contraction during cycling and the failure of NCs to sustain the cyclic strain [55]. On the other hand, the NFs effectively sustain the cyclic strain due to their flexible architecture formed by impregnation of the NFs within the CNS network [56]. The greater morphological stability of NF-based electrode and hence better electron transport can be considered as the primary reason for its higher capacity as compared to NC-based electrode. Figure 13 shows the TEM images and the corresponding SAED patterns of the cycled electrodes. As can be seen, the NF-based electrode is characterized by the formation of NiO crystallites impregnated within CNS. The average size of the crystals, as evident from TEM images, is between 15 and 20 nm which is the same as the individual crystallite size within the NiO NF, Fig. 2a. Also, the indexed SAED pattern corresponds to polycrystalline FCC NiO which shows that the polycrystalline NiO NFs disintegrate into individual crystals during the cycling process. As far as NC-based electrode is concerned, no individual
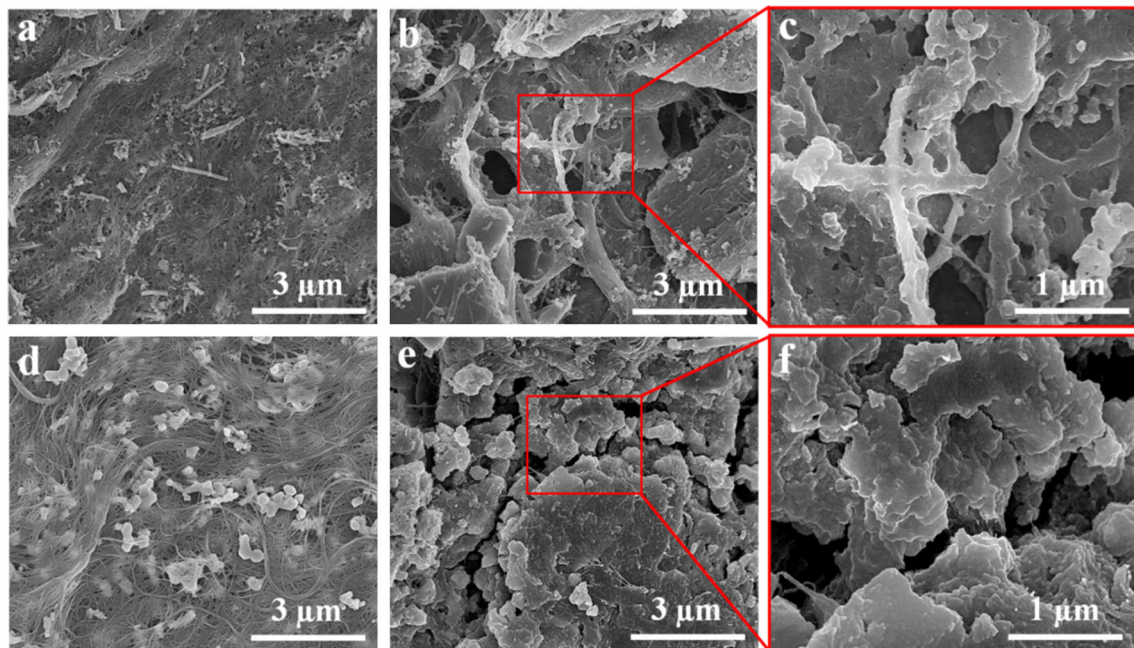

Figure 12 SEM images of fresh **a** NiO NFs/CNS and **d** NiO NCs/CNS electrodes. **b** and **e** after 50 cycles of **a** and **d**, respectively. **c** and **f** are magnified images of **b** and **e**, respectively.
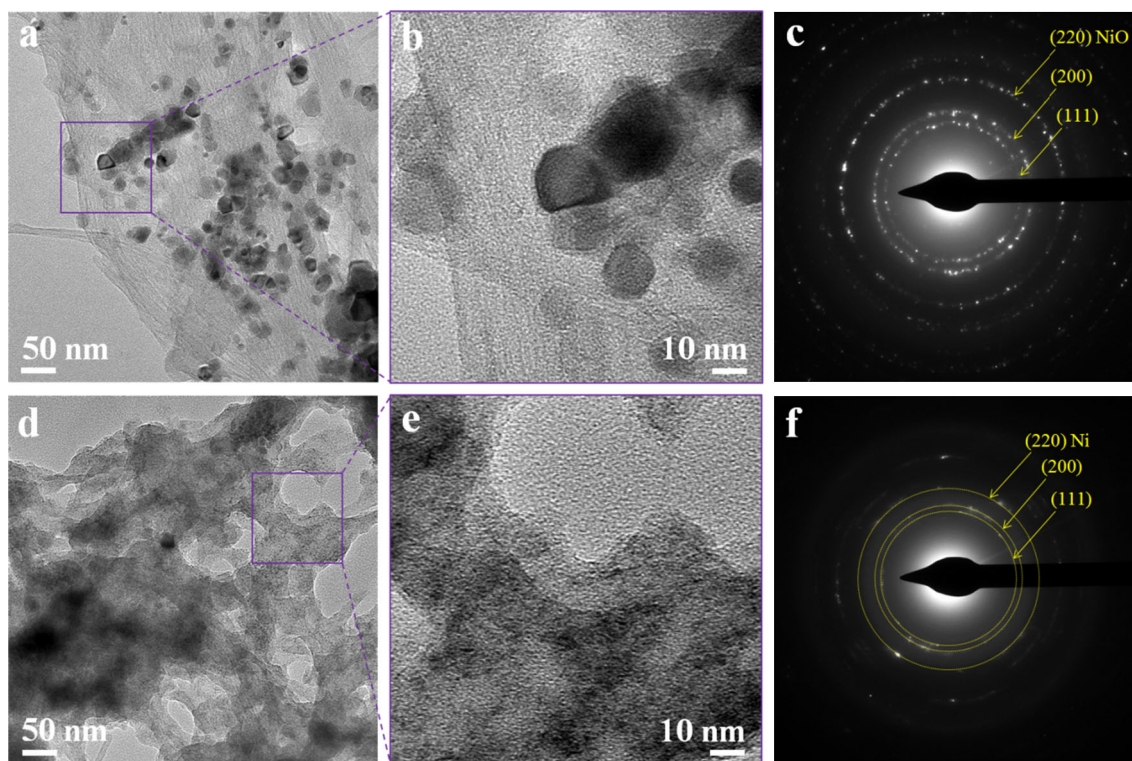
Figure 13 TEM images of **a** NiO NFs/CNS and **d** NiO NCs/CNS electrodes after 50 cycles. **b** and **e** are magnified images of **a** and **d**, respectively. **c** and **f** SAED pattern for **b** and **e**, respectively.

crystallites exist and the NiO NCs completely transformed to Ni which is coated all over the CNS network. Extremely tiny Ni crystallites of size below 5 nm can, however, be observed. The corresponding indexed SAED pattern consisting of diffuse rings corresponds to polycrystalline FCC Ni [57] which shows that the NiO NCs permanently transform to Ni and forming a composite with CNS during repeated cycling. This also explains the more consistent electrochemical performance of NC-based electrodes which permanently transform to Ni-CNS composite as compared to NF-based electrode where the NiO continues to exist even after repeated cycling and hence exhibits more variation between the cycles and strong dependence on the current density during C–D process.

The significant difference in the performance of semi-crystalline NiO NFs and fully crystalline NiO NCs can be explained in terms of their microstructure and surface chemistry. In case of NF-based anode, the key observation is the disintegration of NiO NFs into individual NiO crystallites during repeated cycling. Moreover, these crystallites do not transform to Ni

even after repeated cycling and remain dispersed within the CNS network. Contrary to that, in the anode based on NiO NCs, the repeated cycling causes the permanent transformation of NiO NCs into tiny Ni crystallites which become integrated with CNS network. This transformation of pure and crystalline NiO into Ni crystallites during repeated C–D cycles which has been frequently observed and reported [28, 58] occurs via following reaction:

$$NiO + 2Li + 2e^- <=> 4Ni^0 + Li_2O.$$
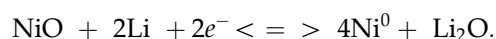
The lack of such conversion in case of NiO NFs can be attributed to their surface chemistry. As shown previously via XPS spectra and the corresponding surface composition, the surface of NFs was found to be O deficient (or Ni rich). When compared with the XPS spectra of various NiO species [59], the XPS spectra of NiO NFs closely match with the NiO–Ni_2O_3 dual-phase system, whereas the XPS spectra of NCs closely match with the two Ni–O systems i.e., monolithic NiO and NiO–NiO($O_{adsorbed}$)-Ni_2O_3 triphase system. This strongly suggests the significant concentration of Ni_2O_3 phase in the NFs which were

treated at lower temperature (475 °C). Although the Ni_2O_3 phase is less likely to exist owing to its lower thermodynamic stability, various studies have reported the existence of Ni_2O_3 at lower temperatures [60–62] and its existence has been attributed to a cation defect-induced formation of Ni^{+3} [63]. Under prolonged high temperature (1000 °C) annealing in air, the defect restoration leads to the formation of thermodynamically stable NiO phase with some possible surface adsorbed O [42], as observed in case of NCs. Thus, in case of polycrystalline NFs, the amorphous region holding the small NiO crystallites and forming the surface is essentially Ni_2O_3 rich. It has also been observed that when the polycrystalline NiO is used as LIB anode, the Ni nucleation preferentially occurs at the grain boundary due to excess energy [64]. Thus, during the repeated cycling, the preferential formation of metallic Ni at the interface of NiO crystallites will lead to the complete elimination of the amorphous region with in the NFs. Since the amorphous part is responsible for holding the crystallites within the NF, the ultimate result will be the complete disintegration of polycrystalline NiO NF into individual NiO crystallites. However, these small NiO crystallites with size 15–20 nm remain integrated within the CNS framework causing minimal electrode cracking during repeated cycling and thus continue to deliver higher capacity [65]. Also, the inverse relation between the current density and specific capacity in case of NFs can be attributed to the incomplete conversion of NiO to Ni when charged at higher current density. In addition, the Ni_2O_3-rich amorphous region surrounding the NiO crystallites may hinder the smooth NiO to Ni conversion leading to inconsistent electrochemical performance during the repeated cycling. In contrast, the highly crystalline NiO NCs transform to Ni during the initial cycles and form one single permanent Ni-CNS composite leading to consistent specific capacity independent of current density. Another important observation in Fig. 8 is the break even at about 420 cycles in the specific capacity of the NFs and NC-based anodes after which the capacity of NCs exceeds the capacity of NFs. This decline in the capacity of NFs which starts from nearly 250th cycle can be attributed to the complete extinction of Ni_2O_3 phase and the permanent transformation of NiO crystallites into Ni which occurs during the early cycling in case on NiO NCs. The continuous increase in capacity in case of NCs after 200 cycles can be attributed to

decrease in the NCs size due to consumption of surface NiO in the relatively large NCs ($\sim$200 nm) leading to net increase in the effective NiO surface area and hence an increased capacity.

Conclusions

In summary, the present work demonstrates the importance of morphology, microstructure, and composition of electrospun NiO nanostructures for their performance as LIB anode. In the form of non-stoichiometric semi-crystalline NFs dispersed within flexible CNS matrix, NiO displays maximum discharge capacity of nearly 700 mAh/g with strong dependence upon the current density. Whereas, in the form of stoichiometric and fully crystalline NCs, it displays maximum discharge capacity of about 500 mAh/g with near independence from the current density. The difference in the electrochemical performance can be attributed to the difference in the microstructure and composition of the electrospun NiO NFs and NCs causing different mechanisms of interaction/reaction with Li ions during C–D process. The NFs which contain significant amorphous content and Ni_2O_3 phase, disintegrate into individual crystallites during repeated cycling and remain impregnated within the CNS network leading to their increased capacity. On the other hand, the fully crystalline NCs transform to Ni during repeated cycling and form a single Ni/CNS composite phase which leads to their decreased capacity. At the same time, the NFs were dependent on the current density, while the NCs were independent. The present work also provides a unique insight into NiO microstructure evolution as a result of its electrochemical interaction with Li ions.

Acknowledgements

References

[1] van Schalkwijk WA, Scrosati B (2002) Advances in lithium-ion batteries. Springer, New York

[2] Pistoia G (1994) Lithium batteries: new materials, developments, and perspectives, vol 5. Elsevier Sci. Ltd., Amsterdam

[3] Etacheri V, Marom R, Elazari R et al (2011) Challenges in the development of advanced Li-ion batteries: a review. Energy Environ Sci 4:3243. doi:10.1039/c1ee01598b

[4] Song M-K, Park S, Alamgir FM et al (2011) Nanostructured electrodes for lithium-ion and lithium-air batteries: the latest developments, challenges, and perspectives. Mater Sci Eng R Rep 72:203–252. doi:10.1016/j.mser.2011.06.001

[5] Poizot P, Laruelle S, Grugeon S et al (2000) Nano-sized transition-metal oxides as negative-electrode materials for lithium-ion batteries. Nature 407:496–499. doi:10.1038/35035045

[6] Bin WuH, Chen JS, Hng HH, Lou XWD (2012) Nanostructured metal oxide-based materials as advanced anodes for lithium-ion batteries. Nanoscale 4:2526–2542. doi:10.1039/c2nr11966h

[7] Li Y, Tan B, Wu Y (2008) Mesoporous Co_3O_4 nanowire arrays for lithium ion batteries with high capacity and rate capability. Nano Lett 8:265–270

[8] Liu H, Wang G, Park J et al (2009) Electrochemical performance of α-Fe_2O_3 nanorods as anode material for lithium-ion cells. Electrochim Acta 54:1733–1736

[9] Fei H, Peng Z, Li L et al (2014) Preparation of carbon-coated iron oxide nanoparticles dispersed on graphene sheets and applications as advanced anode materials for lithium-ion batteries. Nano Res 7:502–510

[10] Bresser D, Mueller F, Fiedler M et al (2013) Transition-metal-doped zinc oxide nanoparticles as a new lithium-ion anode material. Chem Mater 25:4977–4985

[11] Ma F-X, Hu H, Bin WuH et al (2015) Formation of uniform Fe_3O_4 hollow spheres organized by ultrathin nanosheets and their excellent lithium storage properties. Adv Mater 27:4097–4101

[12] Park JC, Kim J, Kwon H, Song H (2009) Gram-scale synthesis of Cu_2O nanocubes and subsequent oxidation to CuO hollow nanostructures for lithium-ion battery anode materials. Adv Mater 21:803–807

[13] Wang C, Zhou Y, Ge M et al (2010) Large-scale synthesis of sno2 nanosheets with high lithium storage capacity. J Am Chem Soc 132:46–47

[14] Liang J, Hu H, Park H et al (2015) Construction of hybrid bowl-like structures by anchoring NiO nanosheets on flat carbon hollow particles with enhanced lithium storage properties. Energy Environ Sci 8:1707–1711

[15] Hu H, Yu L, Gao X et al (2015) Hierarchical tubular structures constructed from ultrathin TiO_2(B) nanosheets for highly reversible lithium storage. Energy Environ Sci 8:1480–1483

[16] Wang Y, Zhang YF, Liu HR et al (2003) Nanocrystalline NiO thin film anode with MgO coating for Li-ion batteries. Electrochim Acta 48:4253–4259. doi:10.1016/S0013-4686(03)00612-1

[17] Wang Y, Qin Q-Z (2002) A Nanocrystalline NiO thin-film electrode prepared by pulsed laser ablation for Li-ion batteries. J Electrochem Soc 149:A873. doi:10.1149/1.1481715

[18] Cheng MY, Hwang BJ (2010) Mesoporous carbon-encapsulated NiO nanocomposite negative electrode materials for high-rate Li-ion battery. J Power Sources 195:4977–4983. doi:10.1016/j.jpowsour.2010.02.059

[19] Needham SA, Wang GX, Liu HK (2006) Synthesis of NiO nanotubes for use as negative electrodes in lithium ion batteries. J Power Sources 159:254–257

[20] Long H, Shi T, Hu H et al (2014) Growth of hierarchal mesoporous NiO nanosheets on carbon cloth as binder-free anodes for high-performance flexible lithium-ion batteries. Sci Rep 4:7413. doi:10.1038/srep07413

[21] Wu MS, Lin YP (2011) Monodispersed macroporous architecture of nickel-oxide film as an anode material for thin-film lithium-ion batteries. Electrochim Acta 56:2068–2073. doi:10.1016/j.electacta.2010.11.089

[22] Sun X, Yan C, Chen Y et al (2014) Three-dimensionally "curved" NiO nanomembranes as ultrahigh rate capability anodes for Li-ion batteries with long cycle lifetimes. Adv Energy Mater. doi:10.1002/aenm.201300912

[23] Su D, Kim H-S, Kim W-S, Wang G (2012) Mesoporous nickel oxide nanowires: hydrothermal synthesis, characterisation and applications for lithium-ion batteries and supercapacitors with superior performance. Chemistry 18:8224–8229. doi:10.1002/chem.201200086

[24] Hyams TC, Bhargava YV, Thorne SA et al (2008) Synthesis of NiO nanowiress for use in lithium batteries. ECS Trans Electrochem Soc 11:1–7. doi:10.1149/1.2953500

[25] Sigmund W, Yuh J, Park H et al (2006) Processing and structure relationships in electrospinning of ceramic fiber systems. J Am Ceram Soc 89:395–407. doi:10.1111/j.1551-2916.2005.00807.x

[26] Ab Kadir R, Li Z, Sadek AZ et al (2014) Electrospun granular hollow SnO_2 nanofibers hydrogen gas sensors operating at low temperatures. J Phys Chem C 118:3129–3139. doi:10.1021/jp411552z

[27] Khalil A, Hashaikeh R (2014) Electrospinning of nickel oxide nanofibers: process parameters and morphology control. Mater Charact 95:65–71. doi:10.1016/j.matchar.2014.06.005

[28] Aravindan V, Suresh Kumar P, Sundaramurthy J et al (2013) Electrospun NiO nanofibers as high performance anode material for Li-ion batteries. J Power Sources 227:284–290. doi:10.1016/j.jpowsour.2012.11.050

[29] Kundu M, Liu L (2015) Electrospun porous nickel oxide nanofibers for high-performance electrochemical energy storage. J Nanosci Lett 5:1–7

[30] Lalia BS, Khalil A, Shah T, Hashaikeh R (2015) Flexible carbon nanostructures with electrospun nickel oxide as a lithium-ion battery anode. Ionics (Kiel). doi:10.1007/s11581-015-1482-3

[31] Khalil A, Hashaikeh R (2015) Electrospun nickel oxide nanofibers: microstructure and surface evolution. Appl Surf Sci 357:1333–1342. doi:10.1016/j.apsusc.2015.09.250

[32] Shah TK, Malecki HC, Basantkumar RR et al (2013) Carbon nanostructures and methods of making the same. US Pat. 20140093728 A1

[33] Vimala Rani JD, Kamatchi S, Dhathathreyan A (2010) Nanoparticles of nickel oxide and nickel hydroxide using lyophilisomes of fibrinogen as template. J Colloid Interface Sci 341:48–52. doi:10.1016/j.jcis.2009.09.006

[34] Chen H, Lu Y, Wu J, Hwang W (2005) Effects of substrate temperature and oxygen pressure on crystallographic orientations of sputtered nickel oxide films. Mater Trans 46:2530–2535

[35] Shukla S, Seal S, Vij R, Bandyopadhyay S (2002) Effect of HPC and water concentration on the evolution of size, aggregation and crystallization of sol-gel nano zirconia. J Nanoparticle Res 4:553–559

[36] Eltejaei H, Towfighi J, Bozorgzadeh HR et al (2011) The influence of preparation conditions on ZrO_2 nanoparticles with different PEG–PPG–PEG surfactants by statistical experimental design. Mater Lett 65:2913–2916. doi:10.1016/j.matlet.2011.06.056

[37] Monnier A, Schüth F, Huo Q et al (1993) Cooperative formation of inorganic-organic interfaces in the synthesis of silicate mesostructures. Science 261:1299–1303

[38] Li L, Krissanasaeranee M, Pattinson SW et al (2010) Enhanced photocatalytic properties in well-ordered mesoporous WO3. Chem Commun 46:7620–7622. doi:10.1039/c0cc01237h

[39] Gebauer D, Liu X, Aziz B et al (2013) Porous tablets of crystalline calcium carbonate via sintering of amorphous nanoparticles. CrystEngComm 15:1257–1263

[40] Saliba N, Parker D, Koel B (1998) Adsorption of oxygen on Au(111) by exposure to ozone. Surf Sci 410:270–282. doi:10.1016/S0039-6028(98)00309-4

[41] Stadnichenko AI, Koshcheev SV, Boronin AI (2007) Oxidation of the polycrystalline gold foil surface and XPS study of oxygen states in oxide layers. Moscow Univ Chem Bull 62:343–349. doi:10.3103/S0027131407060090

[42] Robert T, Bartel M, Offergeld G (1972) Characterization of oxygen species adsorbed on copper and nickel oxides by X-ray photoelectron spectroscopy. Surf Sci 33:123–130

[43] Rajh T, Nedeljkovic JM, Chen LX et al (1999) Improving optical and charge separation properties of nanocrystalline TiO_2 by surface modification with vitamin C. J Phys Chem B 103:3515–3519

[44] Chen LX, Liu T, Thurnauer MC et al (2002) Fe_2O_3 nanoparticle structures investigated by X-ray absorption near-edge structure, surface modifications, and model calculations. J Phys Chem B 106:8539–8546

[45] Khanh BTHL, Hoang VV, Zung H (2008) Structural properties of amorphous Fe_2O_3 nanoparticles. Eur Phys J D 49:325–332. doi:10.1140/epjd/e2008-00168-1

[46] Balbuena PB, Wang YX (2004) Lithium-ion batteries: solid electrolyte interphase. Imperial College Press, London

[47] Boesenberg U, Marcus MA, Shukla AK et al (2014) Asymmetric pathways in the electrochemical conversion reaction of NiO as battery electrode with high storage capacity. Sci Rep 4:7133. doi:10.1038/srep07133

[48] Spinner NS, Palmieri A, Beauregard N et al (2015) Influence of conductivity on the capacity retention of NiO anodes in Li-ion batteries. J Power Sources 276:46–53

[49] Liu L, Li Y, Yuan S et al (2009) Nanosheet-based NiO microspheres: controlled solvothermal synthesis and lithium storage performances. J Phys Chem C 114:251–255

[50] Huang X, Tu J, Zhang C, Xiang J (2007) Net-structured NiO–C nanocomposite as Li-intercalation electrode material. Electrochem Commun 9:1180–1184

[51] Rahman MM, Chou S-L, Zhong C et al (2010) Spray pyrolyzed NiO–C nanocomposite as an anode material for the lithium-ion battery with enhanced capacity retention. Solid State Ion 180:1646–1651

[52] Yuan YF, Xia XH, Wu JB et al (2011) Enhanced electrochromic properties of ordered porous nickel oxide thin film prepared by self-assembled colloidal crystal template-assisted electrodeposition. Electrochim Acta 56:1208–1212. doi:10.1016/j.electacta.2010.10.097

[53] Dalavi DS, Suryavanshi MJ, Patil DS et al (2011) Nanoporous nickel oxide thin films and its improved electrochromic performance: effect of thickness. Appl Surf Sci 257:2647–2656. doi:10.1016/j.apsusc.2010.10.037

[54] Purushothaman KK, Muralidharan G (2011) Enhanced electrochromic performance of nanoporous NiO films. Mater Sci Semicond Process 14:78–83. doi:10.1016/j.mssp.2011.01.014

[55] Wang D, Wu X, Wang Z, Chen L (2005) Cracking causing cyclic instability of $LiFePO_4$ cathode material. J Power Sources 140:125–128. doi:10.1016/j.jpowsour.2004.06.059

[56] Cherian CT, Sundaramurthy J, Reddy MV et al (2013) Morphologically robust $NiFe_2O_4$ nanofibers as high capacity Li-Ion battery anode material. ACS Appl Mater Interfaces 5:9957–9963. doi:10.1021/am401779p

[57] Haslam GE, Chin X-Y, Burstein GT (2011) Passivity and electrocatalysis of nanostructured nickel encapsulated in carbon. Phys Chem Chem Phys 13:12968–12974. doi:10.1039/c1cp20701f

[58] Choi SH, Ko YN, Lee J-K, Kang YC (2014) Rapid continuous synthesis of spherical reduced graphene ball-nickel oxide composite for lithium ion batteries. Sci Rep 4:5786. doi:10.1038/srep05786

[59] Kim KS, Davis RE (1972) Electron spectroscopy of the nickel-oxygen system. J Electron Spectrosc Relat Phenom 1:251–258. doi:10.1016/0368-2048(72)85014-X

[60] Brennan D, Hayward DO, Trapnell BMW (1960) The calorimetric determination of the heats of adsorption of oxygen on evaporated metal films. Proc R Soc Lond A 256:81–105

[61] Wood GC, Wright IG, Ferguson JM (1965) The oxidation of Ni and Co and of Ni/Co alloys at high temperatures. Corros Sci 5:645–661

[62] Venter A, Botha JR (2011) Optical and electrical properties of NiO for possible dielectric applicatons. S Afr J Sci 107:1–6. doi:10.4102/sajs.v107i1/2.268

[63] Goodenough JB (1971) Metallic oxides. Prog Solid State Chem 5:145–399

[64] Lin F, Nordlund D, Weng T-C et al (2014) Phase evolution for conversion reaction electrodes in lithium-ion batteries. Nat Commun 5:3358. doi:10.1038/ncomms4358

[65] Nuli YN, Zhao SL, Qin QZ (2003) Nanocrystalline tin oxides and nickel oxide film anodes for Li-ion batteries. J Power Sources 114:113–120. doi:10.1016/S0378-7753(02)00531-1